

# Enhancing RTK Performance in Urban Environments by Tightly Integrating INS and LiDAR

Xingxing Li, Shiwen Wang, Shengyu Li, Yuxuan Zhou, Chunxi Xia, and Zhiheng Shen

**Abstract**—High-precision and continuous positioning is a fundamental requirement for intelligent navigation applications. Nowadays, the global navigation satellite system (GNSS) real-time kinematic (RTK) technique is recognized as a feasible solution to provide precise positioning services, but its accuracy is susceptible to signal attenuation and will deteriorate drastically in urban environments. Fortunately, the low-cost inertial measurement units (IMU) and light detection and ranging (LiDAR) are available in modern vehicle systems and could be integrated to enhance GNSS performance. In this contribution, aiming to improve RTK performance in GNSS-challenging environments, we propose a tightly coupled RTK/Inertial navigation system (INS)/LiDAR integration method. The GNSS double-differenced pseudorange and carrier-phase measurements, IMU data, and LiDAR plane features are fused at the raw-data level via an extended Kalman filter (EKF). Both simulated tests and real-world experiments were conducted to evaluate the effectiveness of the proposed method. The results indicate that the proposed method is able to achieve sub-decimeter-level accuracy in GNSS-challenging environments, with the improvements of (51.8%, 82.0%, 75.0%) and (53.9%, 71.0%, 41.5%) compared to state-of-the-art LIO-SAM and loosely coupled GNSS/INS/LiDAR integration. Meanwhile, the ambiguity fixing rate could be improved by more than 10% with the assistance of LiDAR plane features. Similar improvements can also be achieved in velocity and attitude estimation.

**Index Terms**—Global Navigation Satellite System, Inertial Navigation System, LiDAR, Urban environment.

## I. INTRODUCTION

ACCURATE, consistent, and continuous navigation solution is in great demand in modern intelligent vehicle systems, such as autonomous driving and unmanned delivery [1] [2]. Since the stand-alone sensor has its inherent limitations and cannot cover all application scenarios, the multi-sensor fusion, which could provide natural robustness to sensor degradation, will be a core component of the vehicle navigation in the near future [3] [4].

Recently, the global navigation satellite system (GNSS) is becoming increasingly popular due to its capability to provide all-weather positioning services, especially after the rapid development of multiple GNSS constellations [5]. The most representative high-precision GNSS technique is real-time

kinematic (RTK), which uses both pseudorange and carrier-phase measurements and could achieve rapid or instantaneous decimeter-level positioning accuracy in open areas with the assistance of base stations [6]. By recovering the carrier-phase ambiguity from float to integer values, which is known as the ambiguity resolution, the positioning accuracy could be further improved to the centimeter-level [7]. The various implementations and analyses of RTK have been extensively studied over the past few decades [8]. However, GNSS signals are susceptible to multipath effects or being blocked, resulting in unreliable and discontinuous observations in urban environments [9].

Fortunately, the inertial navigation system (INS) is self-contained and could provide high-frequency and continuous navigation outputs. Thus, some studies incorporate GNSS with INS to augment the positioning performance in urban environments [10]–[15]. In such a system, GNSS can provide global position information to restrain time-increasing INS errors, while INS could bridge GNSS signal outages and shorten on-the-fly ambiguity search time [10]. The existing work of GNSS/INS integration can be characterized as loosely coupled and tightly coupled methods [11]. Generally, the loosely coupled methods process the measurements from each sensor separately, whose navigation solution could be fragile and discontinuous when the number of available satellites is less than four [12]. In contrast, the tightly coupled methods directly fuse the raw measurements of GNSS and INS, which has been proved to outperform the loosely coupled methods in terms of accuracy and robustness [13], therefore drawing increasing research interests. Nevertheless, the research [14] demonstrated that the navigation errors in GNSS/INS integration would still accumulate without bounds during long-term signal outages, especially when equipped with the low-cost micro-electro-mechanical system (MEMS) inertial measurement units (IMU) [15]. To cope with this case, fusion with additional sensors, such as light detection and ranging (LiDAR), could be helpful.

LiDAR is an exteroceptive sensor that could provide accurate bearing and ranging measurements of surrounding objects for either perception or navigation tasks. With the advances in manufacturing technology, LiDAR has become practical in vehicle navigation applications and has been extensively investigated, in which fruitful outcomes have been gained [16]–[18]. Among them, the iterative closest point (ICP) [16] and its variants [17] [18] are the conventional methods to obtain relative pose estimates between LiDAR scans. These methods are suitable for dense point clouds but still fragile in environments with vertical sparse and circular structures. To address this issue, the authors in [19] proposed a feature-based ICP method to transform the raw LiDAR point clouds

Copyright (c) 2015 IEEE. Personal use of this material is permitted. However, permission to use this material for any other purposes must be obtained from the IEEE by sending a request to pubs-permissions@ieee.org.

Manuscript received 28 June, 2022; revised 4 February, 2023; accepted 13 March, 2023. This work was financially supported by The National Key Research and Development Program of China (2021YFB2501102); The National Natural Science Foundation of China (Grant 41974027); The Sino-German mobility programme (Grant No. M-0054). (Corresponding author: Shengyu Li)

The authors are with School of Geodesy and Geomatics, Wuhan University, Wuhan 430079, China. (e-mail:lishengyu@whu.edu.cn).

Digital Object Identifier (DOI):

into more efficient features such as edges and planes. The literature [20] leveraged the presence of a ground plane in its segmentation and optimization steps to solve the distortion and real-time local pose estimation. To reduce the computational burden in large-scale dense feature matching, the authors in [21] proposed a novel adaptive voxelization method to efficiently search feature correspondence.

On the basis of efficiently processing LiDAR point clouds, many scholars have conducted in-depth research on the integration of GNSS, INS, and LiDAR. The most straightforward approach is to fuse all the pose estimates from individual sensors through a loosely coupled integration. As studied in [22], both RTK and LiDAR were processed separately to provide periodic corrections to suppress the time-increasing velocity errors. Similarly, the literature [23] loosely integrated mature GNSS/INS with LiDAR SLAM to achieve meter-level positioning performance in urban canyons. Apart from filter-based methods, LIO-SAM [24] is an optimization-based method, in which the IMU pre-integration factor, LiDAR odometry factor, and optional GPS position factor are fused to obtain optimal pose estimates through iterative optimization. Although the study of loosely coupled integration of GNSS/INS/LiDAR has made significant progress, it still shows the limitation of inferior performance for its suboptimal condition. Accordingly, to avoid degeneracy and to make the system more robust, the authors in [25] tightly integrated GNSS/INS with 2D LiDAR to achieve decimeter-level positioning accuracy in urban environments by using time-differenced GPS and tactical-grade IMU measurements. In our previous work [26], the LiDAR scan-to-scan geometric constraints were tightly integrated with GNSS carrier-phase observations and IMU outputs. Specifically, each LiDAR constraint was built independently between every two LiDAR scans in the sliding window, whose geometric strength and efficiency are insufficient. Meanwhile, the GNSS submodule employed the precise point positioning (PPP) technique, which is more prone to multipath effects than RTK and can only maintain meter-level positioning accuracy in urban canyons. As studied in [27], the LiDAR features were initialized in advance with high-precision GNSS results in open areas and were then used to construct position constraints in GNSS-degraded environments. The two-stage constraints could be effective but would be greatly restricted when GNSS experiences long-term outages.

Although numerous efforts have been paid to the various implementations of GNSS/INS/LiDAR integrations, most of them mainly focused on the loosely coupled scheme, in which limited support could be used to improve GNSS self-performance in return. As a result, only meter-level positioning accuracy could be achieved. To this end, aiming to achieve accurate and robust navigation in urban environments, we innovatively integrate double-differenced RTK measurements with IMU data and LiDAR plane features in a tightly coupled manner to fully exploit the complementary properties of heterogeneous sensors. The continuously tracked LiDAR plane features could construct strong geometric constraints to prevent inertial sensors from drifting, so as to improve ambiguity fixing rate and positioning accuracy.

The main contributions in this paper are highlighted as

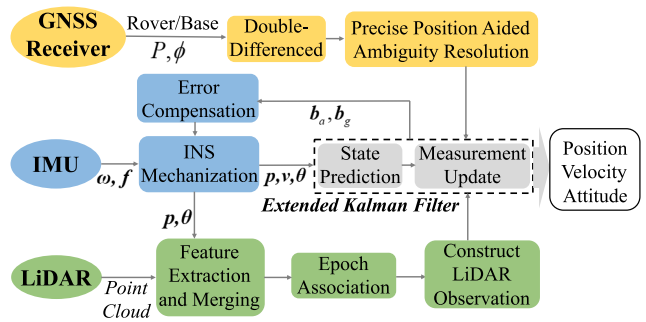


Fig. 1. The pipeline of the proposed tightly coupled GNSS/INS/LiDAR integrated system.

follows:

- We propose a tightly coupled RTK/INS/LiDAR integration method, in which the GNSS double-differenced pseudorange and carrier-phase measurements, MEMS-IMU data, and extracted LiDAR plane features are directly fused at the raw-data level through an extended Kalman filter (EKF). Compared with traditional decoupling methods, the proposed method enables increased robustness to the failure of individual sensors and could enhance RTK self-performance.
- To our best knowledge, it is the first time that continuously tracked LiDAR plane features are utilized to improve the ambiguity fixing rate in the RTK processing. Both theoretical analysis and experimental verification were conducted to evaluate the aiding effect of LiDAR on the carrier-phase ambiguity.
- We perform extensive experimental validations of the proposed method on both simulated tests and real-world experiments, showing that the proposed tightly coupled RTK/INS/LiDAR integration method enables more accurate and robust state estimation than the corresponding loosely coupled methods and state-of-the-art LIO-SAM [24].

The remaining paper is organized as follows: Section II describes the overview of the system. The mathematical models of involved sensors are introduced in Section III. The implementation details of the proposed method and the theoretical analysis of LiDAR aiding effect on ambiguity resolution are presented in Section IV. The simulated tests and real-world experiments are respectively conducted in Section V and Section VI, and the corresponding results are analyzed. Finally, some conclusions are drawn in Section VII.

## II. SYSTEM OVERVIEW

Fig. 1 shows the system structure of the proposed tightly coupled RTK/INS/LiDAR method. As can be seen, IMU is regarded as the core sensor to bridge GNSS and LiDAR submodules for its low fault rate and high sampling frequency. To implement this integrated system, a centralized EKF is employed due to its excellent real-time performance. The high-rate pose prediction obtained by INS mechanization is utilized to aid GNSS outlier detection, LiDAR de-skew as well as

plane-feature association. Once the raw GNSS measurements are available, the double-differenced operations will be performed. Then, the precise prior position information from the integrated system will assist in the ambiguity searching, fixing and its validation. When a new LiDAR scan is recorded, the current LiDAR states (position and attitude) and corresponding covariance will be augmented into the integrated system. The GNSS and LiDAR measurement updates are performed asynchronously to correct the filter states. Finally, the estimated IMU biases will be fed back to compensate next IMU data.

### III. SENSOR MODEL

In this section, the INS dynamic model, RTK measurement model, and LiDAR plane-feature tracking method is introduced. The Earth-Centered, Earth-Fixed (ECEF) frame (e-frame) is chosen as the reference frame in this integrated system, making it easier to use raw GNSS measurements and suppress the effect of the earth's rotation on INS compared to the local-level equivalent methods [28].

#### A. INS Model

In this integrated system, the IMU outputs are used to propagate the system states forward in time, namely INS mechanization. The INS continuous dynamic model can be expressed as:

$$\begin{cases} \delta \dot{\mathbf{p}}^e = \delta \mathbf{v}_b^e \\ \delta \dot{\mathbf{v}}^e = -2(\boldsymbol{\omega}_{ie}^e) \times \delta \mathbf{v}^e + (\mathbf{C}_b^e \mathbf{f}_{ib}^b) \times \delta \boldsymbol{\theta}^e + \mathbf{C}_b^e \delta \mathbf{f}_{ib}^b + \delta \mathbf{g}^e \\ \delta \dot{\boldsymbol{\theta}}^e = -(\boldsymbol{\omega}_{ie}^e) \times \delta \boldsymbol{\theta}^e - \mathbf{C}_b^e \delta \boldsymbol{\omega}_{ib}^b \end{cases} \quad (1)$$

where  $(\cdot) \times$  denotes the skew-symmetric matrix;  $\delta \mathbf{p}^e$ ,  $\delta \mathbf{v}^e$ , and  $\delta \boldsymbol{\theta}^e$  represent the position, velocity, and attitude errors of the body with respect to the e-frame, respectively;  $\mathbf{f}_{ib}^b$  and  $\boldsymbol{\omega}_{ib}^b$  stand for the accelerator and gyroscope outputs, respectively;  $\mathbf{C}_b^e$  denotes the direction cosine matrix from body frame (b-frame) to e-frame;  $\boldsymbol{\omega}_{ie}^e$  represents the angular rate of earth rotation, projected in e-frame;  $\mathbf{g}^e$  is the error vector of gravity in the e-frame.

#### B. RTK Measurement Model

RTK is a widely used differential GNSS (DGNSS) positioning technique, which has the potential to achieve centimeter-level positioning accuracy in open-sky areas. Benefiting from the aiding information provided by the base station, various errors along the signal path can be well eliminated. On this basis, millimeter-level double-differenced pseudorange and carrier-phase measurements could be established. In this work, we follow the standard framework of multi-constellation RTK, which can be derived from undifferenced pseudorange and carrier-phase model as follows [5]:

$$\begin{cases} P = \rho + c(dt_r - dt^s) + Iono + Trop + \varepsilon_P \\ \lambda \Phi = \rho + c(dt_r - dt^s) + \lambda N - Iono + Trop + \varepsilon_\Phi \end{cases} \quad (2)$$

where  $P$  and  $\Phi$  are the pseudorange and carrier-phase measurements, respectively;  $\rho$  is the geometric distance between the receiver  $r$  and satellite  $s$ ;  $dt^s$  and  $dt_r$  denote the clock offsets of the satellite and the receiver, respectively;  $\lambda$  and

$N$  stand for the wavelength and ambiguity of the carrier-phase measurements;  $Iono$  and  $Trop$  represent the ionospheric and tropospheric delay, respectively;  $\varepsilon_P$  and  $\varepsilon_\Phi$  contain the measurement noise and other unmodeled errors.

By performing single differencing between the base station ( $b$ ) and rover station as well as reference satellite ( $S_i$ ) and non-reference satellite ( $S_j$ ), we could obtain the double-differenced measurement model as follows:

$$\begin{cases} \nabla \Delta P_{r,b}^{S_i,S_j} = \nabla \Delta \rho_{r,b}^{S_i,S_j} + \nabla \Delta \varepsilon_{P,r,b}^{S_i,S_j} \\ \lambda \nabla \Delta \Phi_{r,b}^{S_i,S_j} = \nabla \Delta \rho_{r,b}^{S_i,S_j} + \lambda \nabla \Delta N_{r,b}^{S_i,S_j} + \nabla \Delta \varepsilon_{\Phi,r,b}^{S_i,S_j} \end{cases} \quad (3)$$

where  $\nabla \Delta (\cdot)_{r,b}^{S_i,S_j} = \left( (\cdot)_{r,b}^{S_i} - (\cdot)_{r,b}^{S_j} \right) - \left( (\cdot)_r^{S_i} - (\cdot)_r^{S_j} \right)$  denotes the double-differenced operator.

By applying the double-differenced operations in (3), the clock offsets  $dt^s$  and  $dt_r$  can be well eliminated. Furthermore, if the short baseline is less than 5 km, the remaining double-differenced  $Iono$  and  $Trop$  can also be neglected [9].

It is worth mentioning that the phase lock loop (PLL) in the GNSS receiver couldn't directly obtain the starting point of the carrier cycle counter, namely ambiguity  $N$ , which makes the carrier-phase measurements ambiguous. If the ambiguity can be determined correctly, the accuracy of carrier-phase measurements can be further improved to the millimeter-level [29]. Therefore, the correct determination of ambiguity is of great importance for high-precision RTK positioning. To address this issue, the least-square ambiguity decorrelation adjustment (LAMBDA) method is employed in this paper [30], which solves the integer least-squares estimates of ambiguities based on the following objective function:

$$f(\nabla \Delta N) = \min \left\{ (\nabla \Delta \hat{N} - \nabla \Delta N)^\top \mathbf{P}_{\nabla \Delta \hat{N}} (\nabla \Delta \hat{N} - \nabla \Delta N) \right\} \quad (4)$$

where the  $\nabla \Delta \hat{N}$  and  $\mathbf{P}_{\nabla \Delta \hat{N}}$  stand for the real-valued estimates for the ambiguity and corresponding covariance matrix. Once the optimal integer ambiguity  $\nabla \Delta \tilde{N}$  has been obtained, it will be used to revise the receiver position  $\hat{\mathbf{p}}_r$  as below:

$$\tilde{\mathbf{p}}_r = \hat{\mathbf{p}}_r - \mathbf{P}_{\hat{\mathbf{p}}_r, \nabla \Delta \hat{N}} \mathbf{P}_{\nabla \Delta \hat{N}}^{-1} (\nabla \Delta \hat{N} - \nabla \Delta \tilde{N}) \quad (5)$$

where  $\tilde{\mathbf{p}}_r$  and  $\tilde{N}$  are regarded as the "float-solution";  $\hat{\mathbf{p}}_r$  and  $\nabla \Delta \hat{N}$  are the "fixed-solution". Moreover, the ratio test proposed in [30] is used to ensure the accuracy of fixed ambiguity.

#### C. LiDAR Plane-Feature Tracking Model

With rapid development in manufacturing technology, LiDAR has become a feasible option for either navigation or perception tasks. However, traditional methods always come at the cost of computational burden and cumbersome preparation [31]. To address this issue, a modified plane-feature tracking method including extraction, merging, and epoch association is presented to extract the dominant structural information from raw point clouds to construct a more efficient and stable data association between multiple LiDAR scans.

Adhering to [32], a plane feature could be extracted from raw point clouds and represented by a six-degree-of-freedom (6-DOF) vector composed of a center point  $\mathbf{c}$  and a unit normal

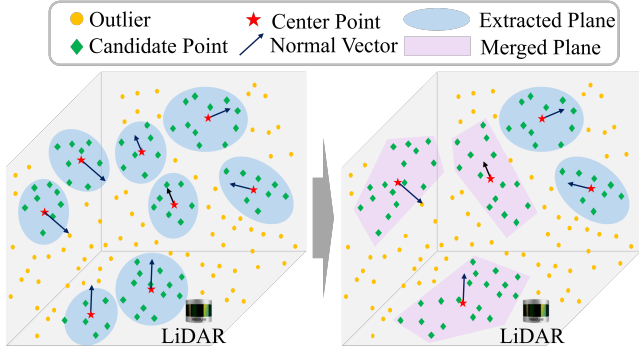


Fig. 2. The simplified models of plane-feature extraction (left) and merging (right).

vector  $\mathbf{u}$ . Generally, the structural information contained in a single plane feature is limited. Meanwhile, many “pony planes” would represent the same surface (e.g., buildings and walls). This data redundancy cannot be ignored as it significantly increases the computational burden. To this end, it is reasonable to merge the plane features belonging to the same surface, which can be completed by constructing the residual as:

$$\mathbf{r}_{s,n} = \begin{bmatrix} \arccos \|\mathbf{u}_s \cdot \mathbf{u}_n\| \\ \mathbf{u}_s^\top (\mathbf{c}_n - \mathbf{c}_s) \\ \mathbf{u}_n^\top (\mathbf{c}_s - \mathbf{c}_n) \end{bmatrix} \quad (6)$$

where the  $\{\mathbf{u}_s, \mathbf{c}_s\}$  and  $\{\mathbf{u}_n, \mathbf{c}_n\}$  are the sparsely selected plane feature and its closest plane feature, respectively. The first row of the residual is the parallelism of the two planes, and both the second and the third rows represent the distance between the two planes.

If the residual is less than the threshold, the corresponding candidate points in the two planes will jointly re-extract a new  $\{\mathbf{u}, \mathbf{c}\}$  following [33]. This process will be repeated several times to ensure the planes that belonged to the same surface are merged as much as possible. The illustration of merging processing is shown in Fig. 2.

Subsequently, the merged plane features will participate in the epoch association between consecutive LiDAR scans. Based on the INS-predicted pose  $\{\mathbf{C}_{l_{pre}}^{l_{cur}}, \mathbf{t}_{l_{pre}}^{l_{cur}}\}$  between current frame  $l_{cur}$  and previous frame  $l_{pre}$ , we could project the plane feature from the previous frame to the current frame to construct a residual to check whether the correspondences can be built.

$$\mathbf{r}_{m,n}^{l_{pre}, l_{cur}} = \begin{bmatrix} \arccos \left\| \mathbf{u}_n^{l_{cur}} \cdot \left( \mathbf{C}_{l_{pre}}^{l_{cur}} \cdot \mathbf{u}_m^{l_{pre}} \right) \right\| \\ \mathbf{u}_n^{l_{cur} \top} \left( \mathbf{c}_n^{l_{cur}} - \mathbf{t}_{l_{pre}}^{l_{cur}} + \mathbf{C}_{l_{pre}}^{l_{cur}} \cdot \mathbf{c}_m^{l_{pre}} \right) \end{bmatrix} \quad (7)$$

where  $\{\mathbf{u}_m^{l_{pre}}, \mathbf{c}_m^{l_{pre}}\}$  and  $\{\mathbf{u}_n^{l_{cur}}, \mathbf{c}_n^{l_{cur}}\}$  represent the  $m^{th}$  plane feature in the previous frame and the  $n^{th}$  plane feature in the current frame, respectively. Once the residual passes the threshold, an epoch association will be built. Noted that the KD-Tree [34] is used for fast indexing in this processing.

## IV. THE TIGHTLY COUPLED RTK/INS/LiDAR INTEGRATED SYSTEM

### A. State Description and Prediction

Based on the sensor models mentioned above, the entire state vector composed of INS state  $\delta \mathbf{x}_{INS}$ , GNSS state  $\delta \mathbf{x}_{RTK}$ , and LiDAR state  $\delta \mathbf{x}_{LiDAR}$  can be described as:

$$\delta \mathbf{x} = \begin{bmatrix} \delta \mathbf{x}_{INS} & \delta \mathbf{x}_{RTK} & \delta \mathbf{x}_{LiDAR} \end{bmatrix}^\top \quad (8)$$

where  $\delta \mathbf{x}_{INS}$  includes the position, velocity, and attitude of the body with respect to the e-frame. Besides, to model the inertial sensor errors, the bias-drifts of accelerator  $\delta \mathbf{b}_a$  and gyroscope  $\delta \mathbf{b}_g$  are also considered, which are modeled as random walk process [35]. Thus, the INS state is defined as:

$$\delta \mathbf{x}_{INS} = \begin{bmatrix} \delta \mathbf{p}^e & \delta \mathbf{v}^e & \delta \boldsymbol{\theta}^e & \delta \mathbf{b}_a & \delta \mathbf{b}_g \end{bmatrix} \quad (9)$$

As for GNSS, the receiver position  $\delta \mathbf{p}_r^e$  can be related to the IMU center, so the estimated parameters in RTK are only the double-differenced ambiguities  $\nabla \Delta \mathbf{N}$  for each observable satellite, which could be represented as follows:

$$\delta \mathbf{x}_{RTK} = \begin{bmatrix} \nabla \Delta \mathbf{N} \end{bmatrix} \quad (10)$$

In terms of LiDAR parameterization, a sliding window of LiDAR poses is maintained for plane-feature geometric constraints. The corresponding states can be written as:

$$\delta \mathbf{x}_{LiDAR} = \begin{bmatrix} \dots & \delta \mathbf{p}_{l_k}^e & \delta \boldsymbol{\theta}_{l_k}^e & \dots \end{bmatrix} \quad (11)$$

where the  $\delta \mathbf{p}_{l_k}^e$  and  $\delta \boldsymbol{\theta}_{l_k}^e$  denote the position and attitude error of LiDAR at epoch  $k$ , respectively. The capacity of the sliding window is pre-defined and the oldest LiDAR frame will be marginalized when the window is full.

In the state prediction, the INS states are propagated forward in time by INS mechanization. The double-differenced ambiguities and the LiDAR poses in the sliding window are regarded as constants without process noises. As for the covariance propagation, it can be calculated by the continuous system model, which can be written as follows:

$$\begin{bmatrix} \delta \dot{\mathbf{x}}_{INS} \\ \delta \dot{\mathbf{x}}_{RTK} \\ \delta \dot{\mathbf{x}}_{LiDAR} \end{bmatrix} = \begin{bmatrix} \mathbf{F}_{INS} & & \\ & \mathbf{0} & \\ & & \mathbf{0} \end{bmatrix} \begin{bmatrix} \delta \mathbf{x}_{INS} \\ \delta \mathbf{x}_{RTK} \\ \delta \mathbf{x}_{LiDAR} \end{bmatrix} + \boldsymbol{\eta} \quad (12)$$

where  $\boldsymbol{\eta}$  is the system noise, which contains the Gaussian noise of the accelerometer and gyroscope. The detailed form of  $\mathbf{F}_{INS}$  can refer to Appendix.

Based on equation (12), the covariance propagation could be expressed as:

$$\mathbf{P}_{(k,k-1)} = \boldsymbol{\phi}_{k,k-1} \mathbf{P}_{(k-1)} \boldsymbol{\phi}_{k,k-1}^\top + \mathbf{Q}_{k-1} \quad (13)$$

where  $\mathbf{Q}_{k-1}$  is the discrete-time noise covariance matrix;  $\boldsymbol{\phi}_{k,k-1}$  is the discrete-time state transition matrix. Once a new LiDAR scan is recorded, the system states would be augmented with a copy of the current LiDAR pose. The corresponding variance is also augmented as follows [36]:

$$\mathbf{P}^*_{(k,k-1)} = \begin{pmatrix} \mathbf{I}_{15+m+6n} \\ \mathbf{J} \end{pmatrix} \mathbf{P}_{(k,k-1)} \begin{pmatrix} \mathbf{I}_{15+m+6n} \\ \mathbf{J} \end{pmatrix}^\top \quad (14)$$

with

$$\mathbf{J} = \begin{pmatrix} \mathbf{I} & \mathbf{0}_{3 \times 3} & (\mathbf{C}_b^{e+ab}) \times & \mathbf{0}_{3 \times (6+m+6n)} \\ \mathbf{0}_{3 \times 3} & \mathbf{0}_{3 \times 3} & -(\mathbf{C}_b^e \mathbf{C}_l^b)^\top & \mathbf{0}_{3 \times (6+m+6n)} \end{pmatrix} \quad (15)$$

where  $m$  and  $n$  represent the number of double-differenced ambiguities and LiDAR poses, respectively;  $\mathbf{J}$  is the Jacobian matrix of the augmented LiDAR pose with respect to the INS states;  $\mathbf{t}_l^b$  and  $\mathbf{C}_l^b$  stand for the extrinsic parameters between LiDAR and IMU, which are accurately calibrated offline following [37].

### B. RTK Measurement Update

Based on equation (3), the residual vector of the double-differenced pseudorange and carrier-phase measurements can be written as:

$$\begin{cases} \delta P = (\nabla \Delta P - \nabla \Delta \hat{P}) \\ \lambda \delta \Phi = \lambda (\nabla \Delta \Phi - \nabla \Delta \hat{\Phi}) \end{cases} \quad (16)$$

where  $(\nabla \Delta P, \nabla \Delta \Phi)$  and  $(\nabla \Delta \hat{P}, \nabla \Delta \hat{\Phi})$  denote the original and INS-predicted GNSS measurements, respectively.

Since that GNSS has a different reference point from IMU center, the lever-arm  $\mathbf{l}_r^b$  should be calibrated in advance and considered in the RTK measurement update, which can be expressed as [38]:

$$\delta \mathbf{p}^e = \delta \mathbf{p}_r^e - (\mathbf{C}_b^e \mathbf{l}_r^b) \times \delta \boldsymbol{\theta}^e \quad (17)$$

By introducing equation (17) into equation (16), the linearized residual vector can be simply written as:

$$\delta \mathbf{r}_{RTK} = \mathbf{H} \delta \mathbf{x}_{INS} + \boldsymbol{\Lambda} \delta \mathbf{x}_{RTK} + \boldsymbol{\varepsilon}_{RTK} \quad (18)$$

with

$$\mathbf{H} = \begin{bmatrix} \frac{\mathbf{p}_r^e - \mathbf{p}^S}{\|\mathbf{p}_r^e - \mathbf{p}^S\|} & \mathbf{0} & \frac{\mathbf{p}_r^e - \mathbf{p}^S}{\|\mathbf{p}_r^e - \mathbf{p}^S\|} (\mathbf{C}_b^e \mathbf{l}_r^b) \times & \mathbf{0} & \mathbf{0} \end{bmatrix} \quad (19)$$

$$\boldsymbol{\Lambda} = \text{diag}(\lambda_1 \quad \dots \quad \lambda_m) \quad (20)$$

where  $\boldsymbol{\varepsilon}_{RTK}$  stand for the measurement noise;  $\mathbf{H}$  and  $\boldsymbol{\Lambda}$  are the Jacobians with respect to INS states and double-differenced ambiguity, respectively.

### C. LiDAR Measurement Update

In Section III, the associated plane-feature correspondence in the sliding window can be obtained. Since the redundant representation of 6-DOP vector  $\{\mathbf{u}, \mathbf{c}\}$  could lead to possible numerical instability, it cannot be directly used in the measurement updates. To address this issue, the traditional plane parameters will be simplified into a 3-DOF vector, which represents the foothold point of the origin to the plane. The relationship between the footholds and the plane features can be described as follows:

$$\boldsymbol{\Gamma} = \mathbf{u} (\mathbf{u}^\top \mathbf{c}) = \mathbf{u} \cdot d \quad (21)$$

where  $d$  is the distance from the origin of the LiDAR frame to the plane.

Then, we can use the INS-predicted pose estimates to construct the relationship of associated plane features as:

$$\begin{aligned} \boldsymbol{\Gamma}_{i,j}^{l_{pre}, l_{cur}} &= \mathbf{u}_{i,j} \cdot d_{i,j} \\ &= (\mathbf{C}_{l_{pre}}^{l_{cur}} \mathbf{u}_i^{l_{pre}}) \left[ d_i^{l_{pre}} - (\mathbf{C}_{l_{pre}}^{l_{cur}} \mathbf{t}_{l_{pre}}^{l_{cur}})^\top \mathbf{u}_i^{l_{pre}} \right] \end{aligned} \quad (22)$$

where  $i$  and  $j$  represent the index of the associated plane features, respectively;  $\mathbf{u}_{i,j}^{l_{pre}, l_{cur}}$  is the plane feature projected from the previous to the current LiDAR epoch.

By linearizing equation (22), we have:

$$\begin{aligned} \delta \mathbf{r}_{LiDAR}^{i,j} &= \boldsymbol{\Gamma}_{i,j}^{l_{pre}, l_{cur}} - \hat{\boldsymbol{\Gamma}}_{i,j}^{l_{pre}, l_{cur}} \\ &= \mathbf{H}_{LiDAR}^{i,j} \delta \mathbf{x}_{LiDAR} + \mathbf{H}_{\boldsymbol{\Gamma}}^{i,j} \delta \boldsymbol{\Gamma} + \boldsymbol{\varepsilon}_{LiDAR}^{i,j} \end{aligned} \quad (23)$$

where  $\mathbf{H}_{LiDAR}^{i,j}$  and  $\mathbf{H}_{\boldsymbol{\Gamma}}^{i,j}$  are the Jacobians with respect to the LiDAR states and the 3-DOF plane features, respectively;  $\boldsymbol{\varepsilon}_{LiDAR}^{i,j}$  is the measurement noise. By stacking the residual of all the associated plane features, we have:

$$\delta \mathbf{r}_{LiDAR} = \mathbf{H}_{LiDAR} \delta \mathbf{x}_{LiDAR} + \mathbf{H}_{\boldsymbol{\Gamma}} \delta \boldsymbol{\Gamma} + \boldsymbol{\varepsilon}_{LiDAR} \quad (24)$$

To decorrelate the plane feature with LiDAR poses, the  $\delta \boldsymbol{\Gamma}$  is projected to its null space following [36], which can be written as:

$$\delta \bar{\mathbf{r}}_{LiDAR} = \mathbf{A}^\top \mathbf{H}_{LiDAR} \delta \mathbf{x}_{LiDAR} + \mathbf{A}^\top \boldsymbol{\varepsilon}_{LiDAR} \quad (25)$$

To ensure the robustness of LiDAR measurement update, the Chi-square test is carried out to reject plane-feature outliers [39].

### D. LiDAR Aiding Effect on Ambiguity Resolution

Although the idea of integrating more sensors to improve positioning performance is quite straightforward, the underlying reasons are still worth exploring. Since the RTK self-performance is closely correlated to ambiguity resolution, the detailed theoretical analysis of LiDAR aiding effect on ambiguity resolution is presented in this section.

For simplicity, we assume that the measurement error can be expressed as the product of the error coefficients and corresponding weight. The weights of different GNSS measurements are determined by their satellite elevations and can be expressed with a simplified weight matrix  $\mathbf{W}$ , while LiDAR observations are considered to be equal-weighted. Thus, the measurement noise  $\mathbf{R}$  can be written as:

$$\mathbf{R} = \text{diag}(\sigma_P^2 \cdot \mathbf{W} \quad \sigma_\phi^2 \cdot \mathbf{W} \quad \sigma_L^2 \cdot \mathbf{I}) \quad (26)$$

where the  $\sigma_P$ ,  $\sigma_\phi$  and  $\sigma_L$  represent the noise coefficient of pseudorange, carrier-phase, and LiDAR plane features, respectively. Based on the standard EKF routines, the relationship between prior state covariance  $\mathbf{P}_{(k,k-1)}$  and posterior state covariance  $\mathbf{P}_{(k)}$  can be expressed as:

$$\mathbf{P}_{(k)}^{-1} = \mathbf{P}_{(k,k-1)}^{-1} + \mathbf{H}_k^\top \mathbf{R}^{-1} \mathbf{H}_k \quad (27)$$

Taking the  $i^{\text{th}}$  GNSS measurement and corresponding wavelength  $\lambda_i$  as an example, the ambiguity covariance before integrating with LiDAR can be expressed as follows:

$$\overline{P_{k, \nabla \Delta N, i}} = \frac{\sigma_\phi^2}{\lambda_i^2} \left( w_i + \frac{\sigma_P^2}{\sigma_\phi^2} \alpha_i (\alpha_i^\top w_i^{-1} \alpha_i)^{-1} \alpha_i^\top \right) \quad (28)$$

That after integrating with LiDAR can be written as:

$$\begin{aligned} \overline{P_{k, \nabla \Delta N, i}}' &= \\ \frac{\sigma_\phi^2}{\lambda_i^2} \left( w_i + \frac{\sigma_P^2}{\sigma_\phi^2} \alpha_i (\alpha_i^\top w_i^{-1} \alpha_i + \frac{\sigma_P^2}{\sigma_L^2} h_L^\top h_L)^{-1} \alpha_i^\top \right) \end{aligned} \quad (29)$$

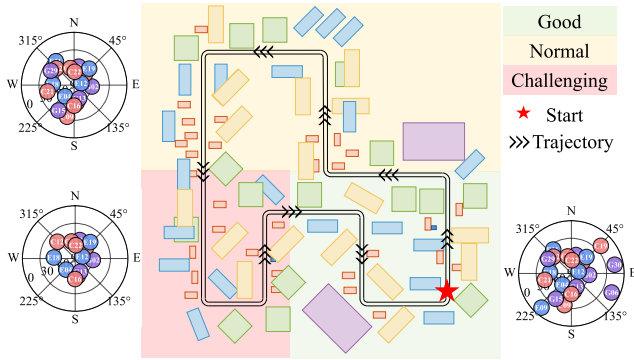


Fig. 3. The simulated scenario and distribution of satellite constellations.

where the  $\alpha_i$  and  $h_L$  are the corresponding measurement coefficient of GNSS and LiDAR, respectively;  $w_i$  is the noise weight of the  $i^{th}$  GNSS measurement.

The ambiguity dilution of precision (ADOP) is widely used to reflect the accuracy of float ambiguity estimates [40], which can be calculated by:

$$ADOP = \sqrt{\det(\mathbf{P}_{\nabla\Delta N})}^{\frac{1}{n}} \quad (30)$$

In the light of equations (26), (27), and (28), we can infer that the ADOP is reduced after the introduction of LiDAR plane features:

$$ADOP_{After} < ADOP_{Before} \quad (31)$$

The authors in [30] have demonstrated that smaller ADOP has a positive effect on faster ambiguity convergence and higher position accuracy. In other words, the more precise the float ambiguity estimate is, the higher the ambiguity fixing rate and better RTK performance will be. Consequently, the theoretical analysis above shows that the enhancement effect of LiDAR aiding effect on RTK is interpretable.

## V. SIMULATED TEST

The simulated tests were first carried out to evaluate the proposed integrated system. As shown in Fig. 3, a simulated

TABLE I  
THE CONFIGURATION OF THE SIMULATED TEST. THREE SETS OF PARAMETERS OF NSAT AND NOISE DENOTE THE GNSS CONFIGURATIONS OF THE “GOOD”, “NORMAL” AND “CHALLENGING” SEGMENTS, RESPECTIVELY

	Average NSAT	27/21/14
GNSS	Pseudorange noise (m)	0.3/1.0/1.3
	Carrier-phase noise (m)	0.003/0.010/0.013
	Observation model	Double-Differenced
	Sampling rate (Hz)	100
IMU	Angle random walk ( $^{\circ}/\sqrt{hr}$ )	0.5
	Velocity random walk ( $m/s/\sqrt{hr}$ )	0.1
	Gyroscope drift ( $^{\circ}/hr$ )	$N(0, 200^2)$
	Accelerator bias (mGal)	$N(0, 2000^2)$
LiDAR	Sampling rate (Hz)	10
	Maximum range (m)	100
	Range accuracy (m)	0.02
	Elevation Resolution ( $^{\circ}$ )	2.5
	Field of view (Horizontal) ( $^{\circ}$ )	[0 360]
	Azimuth Resolution ( $^{\circ}$ )	0.16
	Field of view (Vertical) ( $^{\circ}$ )	[-20 20]

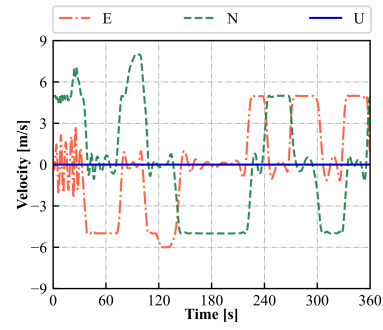


Fig. 4. The time series of velocity in the simulated test.

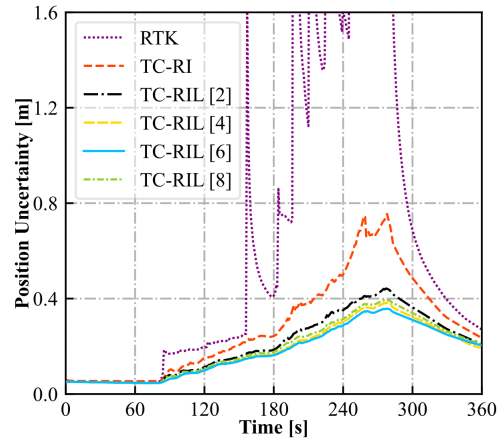


Fig. 5. The time series of position uncertainties for RTK, TC-RI, and TC-RIL in the simulated test. The dark blue, yellow, blue, and green lines denote the TC-RIL integrations with the sliding window sizes of 2, 4, 6, and 8, respectively.

urban scenario including roads and buildings was constructed based on the Scenario Canvas of MATLAB Toolbox. According to the GNSS observing conditions, the simulated trajectory can be categorized into three segments: “Good”, “Normal” and “Challenging”, in which the numbers of available satellites are 27, 21, and 14, respectively. Based on the simulated vehicular scenario, the raw GNSS measurements, IMU data, and LiDAR point clouds are generated with different noise levels. The overall simulated configuration for different sensors is listed in Table I. As evident from the time series of vehicle velocity in Fig. 4, the simulated experiment lasts about 360 s and the velocity varies from 5 m/s to 10 m/s. It should be noted that the vertical speed of the vehicle is maintained at 0 m/s, which is consistent with the real-world urban roads without noticeable height difference.

Attention is first paid to the time series of position uncertainties, which is shown in Fig. 5. There are three configurations considered for comparison and analysis: 1) stand-alone RTK, 2) tightly coupled RTK/INS integration (abbreviated as TC-RI), and 3) tightly coupled RTK/INS/LiDAR integration (abbreviated as TC-RIL). It can be seen that the position uncertainty of RTK increases rapidly in the “Challenging” area. After the inclusion of INS, the corresponding uncertainty decreases notably. When integrated with both IMU data and

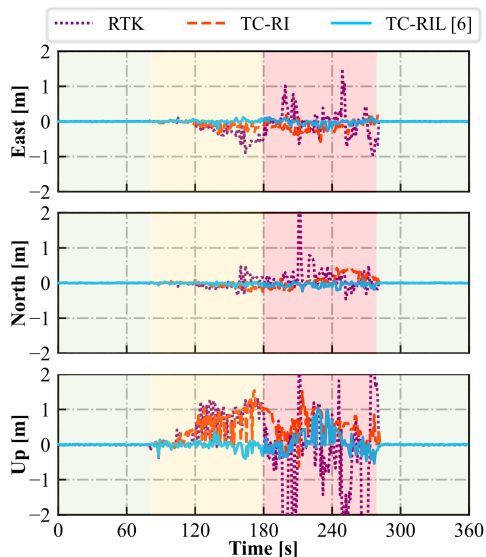


Fig. 6. The position errors of RTK, TC-RI, and TC-RIL in the east, north, and up directions, the sliding window size in TC-RIL is set to 6.

LiDAR plane features, the position uncertainty has a further decline, which indicates that additional LiDAR information could provide extra observability for position estimation. It can be found that the increasing LiDAR sliding window size could bring about limited improvement. This is reasonable since the large size of the sliding window makes it difficult to construct effective epoch associations. Moreover, the position uncertainties begin to converge when the vehicle returns from the “Challenging” area to the “Good” area. The fastest convergence of position uncertainty in TC-RIL also reflects the extra observability provided by plane features.

Since the uncertainty may not truly reflect the performance of the state estimation, the time series of position errors for RTK, TC-RI, and TC-RIL are also presented in Fig. 6. Obviously, RTK could achieve high-precision positioning accuracy in open-sky conditions, but it degrades to meter-level accuracy when the visible satellites significantly reduce in the “Normal” area. While in the “Challenging” area, even the TC-RI is prone to degradation. The maximum position errors of the east, north, and vertical components are 0.579 m, 0.442 m, and 1.542 m in TC-RI, respectively. Comparatively, the corresponding position errors of TC-RIL decrease to 0.276 m, 0.236 m, and 1.039 m. According to the root mean square error (RMSE) and ambiguity fixing rate listed in Table II, the position RMSEs reduced from 0.113 m, 0.113 m, and 0.492 m

TABLE II

THE RMSES OF POSITION, YAW, AND AMBIGUITY FIXING RATE OF RTK, TC-RI, AND TC-RIL IN THE SIMULATED TEST

	Position RMSE (m)			Yaw RMSE (deg)	Fixing Rate
	East	North	Up		
RTK	0.265	0.237	0.962	/	60.6%
TC-RI	0.131	0.113	0.492	0.39	63.3%
TC-RIL	0.046	0.048	0.199	0.09	85.6%

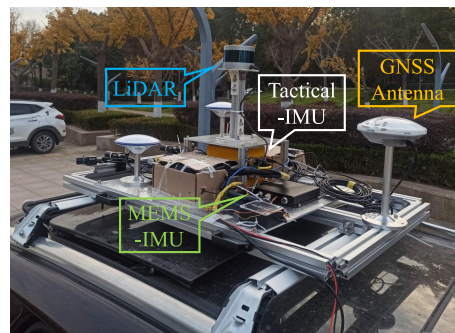


Fig. 7. Overview of the hardware platform.

for the east, north, and vertical components of TC-RI to 0.046 m, 0.048 m, and 0.199 m of TC-RIL. For the ambiguity fixing rate, TC-RIL could achieve a satisfactory ambiguity fixing rate of 85.6%, with improvements of 25.0% and 22.2% with respect to RTK and TC-RI, respectively. Such improvement mainly benefits from the direct position constraints provided by accurate plane-feature correspondences across the sliding window. Moreover, the introduction of LiDAR also brings higher accuracy of attitude estimates, whose RMSE reduces from 0.39° to 0.09°.

## VI. REAL-WORLD EXPERIMENTS

### A. Experimental Description

In order to further validate the feasibility of the proposed TC-RIL system, vehicular field experiments were conducted at Wuhan University on 27 November 2021. As shown in Fig.7, the hardware platform is equipped with a GNSS receiver (Septentrio PolaRx5), a MEMS-IMU (ADIS-16470), and a LiDAR (Velodyne VLP-16). A Tactical-grade IMU (Starneto XW-GI7660) was also installed on the platform for generating reference solutions. Moreover, another Septentrio PolaRx5 GNSS receiver with the antenna was rigidly installed on the rooftop of the School of Geodesy and Geomatics as a reference station for RTK. The performance specifications of the two IMUs are shown in Table III. The sampling rates of the GNSS receiver, MEMS-IMU, Tactical-IMU, and LiDAR were 1 Hz, 100 Hz, 200 Hz, and 10 Hz, respectively. In addition, the GNSS-IMU lever-arm and IMU-LiDAR extrinsic parameters were also pre-calibrated in advance. As for the time synchronization, the pulse per second (PPS) signal generated by the GNSS receiver was used to trigger other sensors and unify their time systems to GPS time at the hardware level. To make a fair comparison, a post-processing software Inertial Explorer 8.9 was employed to calculate the forward-backward

TABLE III

THE PERFORMANCE SPECIFICATIONS OF THE TWO IMUS

IMU	Bias		Random Walk	
	Gyro (°/hr)	Acc. (mGal)	Angular (°/√hr)	Velocity (m/s/√hr)
XW-GI7660	0.3	100	0.01	/
ADIS-16470	8	1300	0.34	0.037



Fig. 8. The top view of the vehicle trajectory and various scenarios in the real-world experiment.

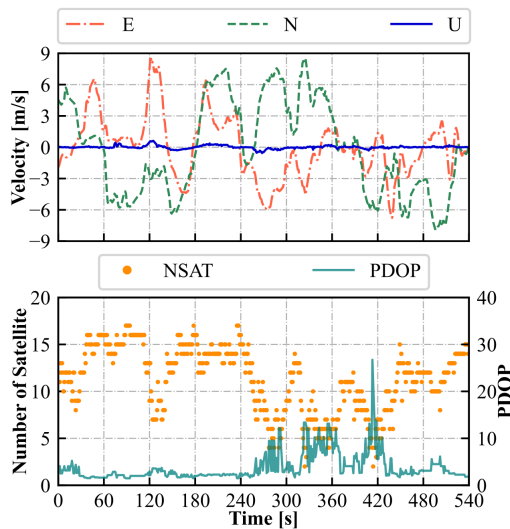


Fig. 9. The time series of velocity and the GNSS visibility in the real-world experiment.

smoothed RTK/Tactical-IMU tightly integrated solution as the reference in the experiment.

Based on the field test trajectory shown in Fig. 8, the vehicle started moving from an open-sky scenario with few trees, low buildings, and wide roads, then ran through the urban canyon, where tall buildings made it difficult to track satellite signals continuously. In the second half of the experiment, frequent signal blockages further challenged GNSS positioning as the vehicle moved into the forest canopy shaded by dense trees. Consequently, the proposed methods can be fully tested in this real-world experiment.

The time series of vehicle velocity and the GNSS visibility during the whole experiment are shown in Fig. 9. The vehicle showed frequent acceleration and deceleration in the horizontal direction, which could provide sufficient excitation for IMU. As for GNSS visibility, even with the inclusion of the GPS,

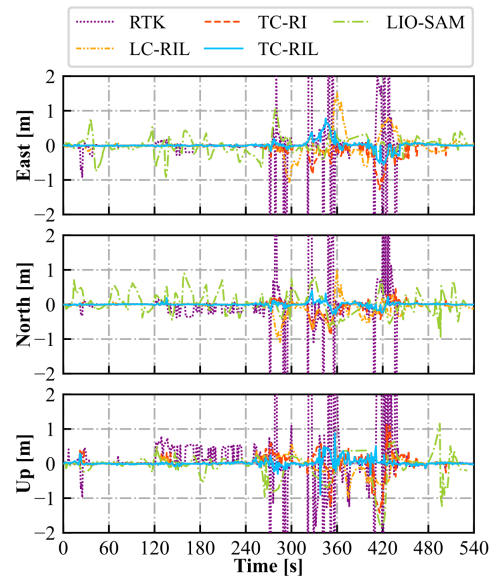


Fig. 10. The time series of position errors for RTK, TC-RI, LC-RIL, TC-RIL and LIO-SAM in the east, north, and up directions.

BDS, and Galileo systems, the average number of available satellites was only 11.3 and the average PDOP (Position Dilution of Precision) was 3.67, which reflects the poor GNSS observing condition. It is worth mentioning that in the forest canopy, the number of visible satellites decreased greatly and the PDOP rose rapidly, which could cause huge challenges for precise positioning. Since the whole experiment was carried out at Wuhan University and the baseline was limited within 3 km, the double-differenced tropospheric and ionospheric delay can be ignored. As for LiDAR, the size of the sliding window was set to 6 to ensure stable plane-feature association as described in Section V.

### B. Result Analysis

To comprehensively verify the performance of different methods, the loosely coupled RTK/INS/LiDAR integration (abbreviated as LC-RIL) and state-of-the-art LIO-SAM [24], which both use position results from stand-alone RTK module for fusion, are also considered in real-world experiments. The time series of position errors for different methods are illustrated in Fig. 10. It can be seen that the stand-alone RTK performance deteriorated to meter-level during the time period from 240 s to 480 s, especially in the forest canopy. As shown in Fig. 9, the deterioration is mainly caused by the lack of visible satellites and short-term signal interruptions. By integrating RTK with INS, the gross errors over 2 m could be eliminated to some extent. However, the rapid error accumulation during long-term GNSS outages is still unavoidable, especially when equipped with MEMS-IMU with high noise levels and unstable biases. Fortunately, the introduction of LiDAR could significantly improve the accuracy and stability of TC-RI, which could be contributed to the strong geometric constraints constructed by the extracted plane features. Interestingly, the LC-RIL performs much worse than TC-RIL, even worse than TC-RI in some periods. The main reason could be the lack

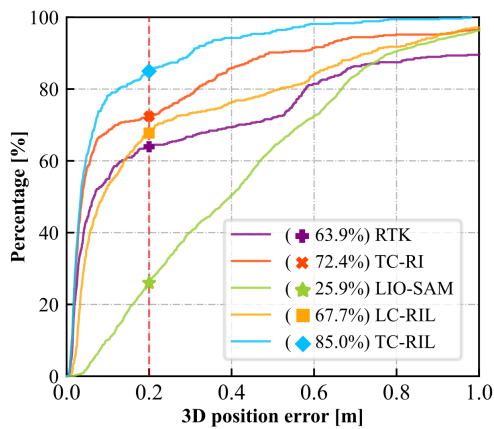


Fig. 11. The CDFs of 3D position errors for RTK, TC-RI, LC-RIL, TC-RIL, and LIO-SAM.

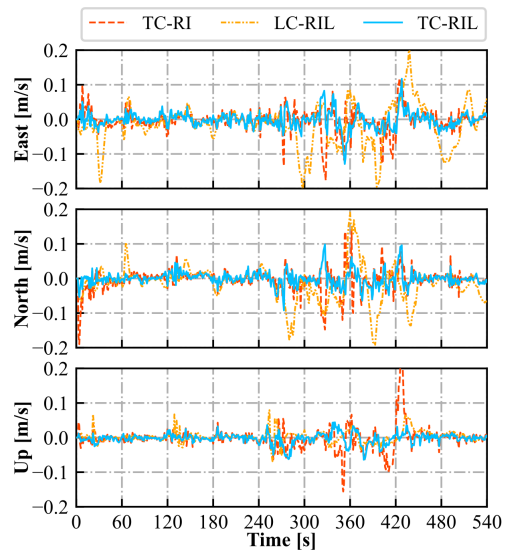


Fig. 12. The time series of velocity errors for TC-RI, LC-RIL, and TC-RIL in the east, north, and up directions.

of robustness against possible outliers in loosely coupled integration. As for optimization-based methods, LIO-SAM could achieve considerable accuracy to TC-RIL in GNSS-degraded environments, but its performance is worse than pure RTK for the first 300 s in open-sky environments. This phenomenon is mainly caused by the fact that the GNSS positioning results are only used when the covariance of estimated positions becomes larger than that of received GNSS information. Considering this, the periodic correction of position errors for LIO-SAM in Fig. 10 is reasonable.

The overall position RMSEs for different methods are listed in Table IV. Influenced by several signal blockages, RTK presents sub-meter-level positioning accuracy. With the inclusion of INS, the position RMSEs reduce to 0.197 m, 0.132 m, and 0.259 m in the east, north, and up components. When both LiDAR information and tight integration are used, the positioning accuracy is the highest among all methods, with improvements of (51.8%, 82.0%, 75.0%) and (53.9%, 71.0%, 41.5%) with respect to LIO-SAM and LC-RIL. Moreover, the pure RTK could achieve ambiguities to be fixed in 383 epochs out of a total of 541 epochs. Since both LC-RIL and LIO-SAM directly use GNSS position results from stand-alone GNSS module, they own the same ambiguity fixing rate as pure RTK at 70.8%. Benefiting from the tightly coupled integration, the prior precise position information derived from INS mechanization could assist in GNSS cycle slip and outlier detection, thereby improving the ambiguity fixing rate

to 76.5%. By introducing LiDAR plane features to further improve the accuracy of INS-predicted pose estimates, the highest ambiguity fixing rates with 86.6% can be achieved among all methods.

To further evaluate the positioning accuracy, the cumulative distribution functions (CDF) of the 3D position errors are also analyzed. The errors within 0.2 m are concerned as their distribution depends heavily on the effectiveness of “fixed solutions”. According to the statistics shown in Fig. 11, LC-RIL improves the distribution of errors within 0.2 m by only 3.8% compared to RTK. As the GNSS is used as a stand-alone submodule, it is difficult for LiDAR to influence the performance of ambiguity resolution. In this case, LiDAR-aided information in the loosely coupled integration has limited improvement in positioning accuracy, especially when fusing with accurate GNSS positioning results. Comparatively, TC-RI can make full use of the raw GNSS measurements and enhance RTK self-performance to achieve a higher ambiguity fixing rate, resulting in an 8.5% improvement in the distribution of errors within 0.2 m. Furthermore, the relative geometric constraints of LiDAR plane features could help reject possible GNSS gross errors and maintain high-precision extrapolated navigation outputs to wait for accurate and reliable GNSS information. Therefore, the introduction of LiDAR plane features into TC-RI enables increased robustness to failure of RTK, especially in urban environments, leading to a 21.1% improvement of errors within 0.2 m. Interestingly, the CDF of LIO-SAM shows a steady upward trend, due to the incremental smoothing of pose graph optimization. However, the distribution of errors within 0.2 m for LIO-SAM is only 26.0% because GNSS is considered as a loop closure factor rather than global position information, resulting in a worse performance than RTK. This corresponds to the frequent jumps of LIO-SAM in Fig. 10.

Similar to position, noticeable velocity improvement can be

TABLE IV

THE POSITION RMSEs AND AMBIGUITY FIXING RATES OF RTK, TC-RI, LC-RIL, TC-RIL, AND LIO-SAM

	Position RMSE (m)			Fixing Rate
	East	North	Up	
RTK	0.844	0.855	1.022	70.8%
TC-RI	0.197	0.132	0.259	76.5%
LIO-SAM	0.276	0.334	0.428	70.8%
LC-RIL	0.289	0.207	0.183	70.8%
TC-RIL	0.133	0.060	0.107	86.6%

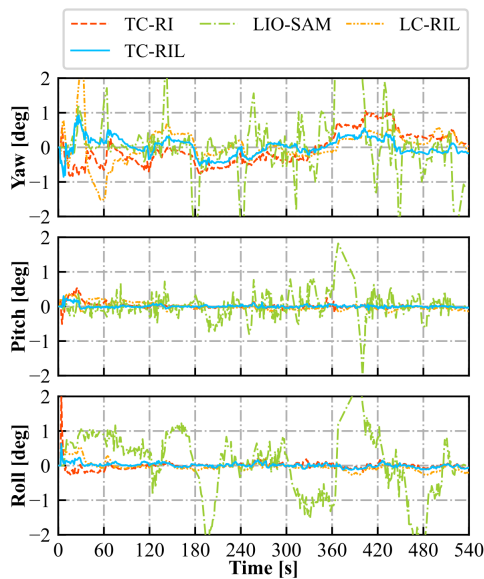


Fig. 13. The time series of attitude errors for TC-RI, LC-RIL, TC-RIL, and LIO-SAM in the east, north, and up directions.

obtained with LiDAR-aided information. Fig. 12 gives out the velocity errors of various methods. Noted that the velocity indicator of LIO-SAM is neglected for the lack of outputs. The velocity errors of TC-RI and LC-RIL frequently increase above 0.2 m/s during the time period of 240 s to 480 s when crossing the forest canopy. Comparatively, the error of TC-RIL keeps within 0.1 m/s and exhibits insignificant degradation. Based on the RMSEs of the velocity shown in Table V, the statistics indicate that the RMSEs of TC-RIL are 0.024 m/s, 0.021 m/s, and 0.015 m/s, respectively, showing improvements of (59.3%, 58.8%, 11.8%) compared with LC-RIL.

Autonomous driving not only requires high-precision positioning results but also relies on accurate attitude information. The time series of the attitude error for different methods are presented in Fig. 13 and the corresponding attitude RMSEs are calculated in Table VI. As can be seen, the estimate of yaw angle underperforms the roll and pitch angles among

TABLE V  
THE VELOCITY RMSEs OF TC-RI, LC-RIL, AND TC-RIL

	Velocity RMSE (m/s)		
	East	North	Up
TC-RI	0.033	0.032	0.033
LC-RIL	0.059	0.051	0.017
TC-RIL	0.024	0.021	0.015

TABLE VI  
THE ATTITUDE RMSEs OF TC-RI, LC-RIL, TC-RIL, AND LIO-SAM

	Attitude RMSE (°)		
	Yaw	Pitch	Roll
TC-RI	0.47	0.10	0.26
LIO-SAM	0.70	0.33	0.88
LC-RIL	0.50	0.11	0.15
TC-RIL	0.29	0.06	0.14

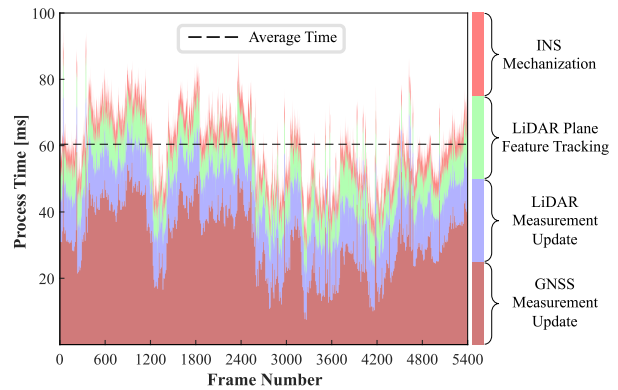


Fig. 14. Detailed processing time of each module.

all methods due to its weak observability in LiDAR-Inertial system. Meanwhile, the roll and pitch angles can be recovered from the LiDAR plane features and IMU measurements alone. As Table VI depicts, the attitude RMSEs of LIO-SAM are  $0.70^\circ$ ,  $0.33^\circ$ , and  $0.88^\circ$  for the yaw, pitch, and roll angles, respectively. Compared to LIO-SAM, TC-RI and LC-RIL upgrade the attitude estimates with the improvement of (32.9%, 69.7%, and 70.5%) and (28.6%, respectively) 66.7%, and 83.0%, respectively. Our proposed TC-RIL achieves the highest attitude accuracy with  $0.29^\circ$ ,  $0.06^\circ$ , and  $0.14^\circ$  in the yaw, pitch, and roll angles. Such improvements are mainly due to the fact that LiDAR plane features can provide direct bearing measurements to slow the drift of attitude errors.

### C. Efficiency Analysis

In addition to the accuracy evaluation, the computation efficiency of TC-RIL is tested on a laptop PC with Intel i7-10875H CPU at 2.30 GHz and 16 GB of RAM. Fig. 14 shows the detailed processing time of our proposed TC-RIL method, which can be mainly divided into INS mechanization module, LiDAR plane feature tracking module, LiDAR and GNSS measurement update modules. The average processing time in one epoch is only 60.4 ms and the maximum processing time is 93.7 ms. It can be seen that the major time-consuming part is the GNSS measurement update as the position information is further utilized in the ambiguity searching and fixing. Due to the 10Hz sampling rate of Velodyne VLP-16, the maximum available processing time in the real-time mode is 100 ms. Thus, our proposed method can achieve real-time performance, and free up more available time for other tasks, such as planning and decision-making.

TABLE VII  
AVERAGE PROCESSING TIME OF LiDAR WITH DIFFERENT SLIDING WINDOW SIZES

Window Size	2	4	6	8
Feature Tracking [ms]	2.9±0.5	4.5±0.8	6.2±1.2	7.4±1.5
Measurement Update [ms]	15.4±0.7	14.1±1.2	14.3±1.2	14.0±1.3

To further explore the impact of different sliding window sizes on computational efficiency, the average processing time of LiDAR with different sliding window sizes is given in TABLE VII. It can be seen that the processing time of LiDAR feature tracking increases with larger window sizes since the system needs to handle more geometric constraints between frames in the sliding window. Although the expansion of sliding window clones more LiDAR states to be estimated, the plane feature correspondence that can be built across the whole sliding window also decreases. This leads to the phenomenon that the linear growth in processing time does not appear in the LiDAR measurement update. As expected, the processing time under different sizes of sliding window is roughly the same, which only occupies 25% of the real-time benchmark.

## VII. CONCLUSION

In order to meet the increasing demand for high-precision positioning for modern navigation applications in urban environments, we propose a tightly coupled RTK/INS/LiDAR integration method. The LiDAR aiding effect on ambiguity resolution is investigated through theoretical analysis. Both simulated tests and real-world experiments were conducted to evaluate the effectiveness of the proposed method. The results indicate that TC-RIL is able to maintain centimeter-level positioning accuracy in open-sky environments and decimeter-level accuracy in challenging environments, which outperforms the loosely coupled methods and state-of-the-art LIO-SAM.

However, several aspects still need to be considered in the future. First, it is necessary to develop the multi-data mutual inspection mechanism to ensure the system robustness. Second, the integration with more sensors involved in intelligent vehicle applications, such as camera and odometer, would be investigated to further improve the positioning performance of the system.

## ACKNOWLEDGMENT

The algorithm implementation is based on the GREAT (GNSS+ REsearch, Application and Teaching) software developed by the GREAT Group, School of Geodesy and Geomatics, Wuhan University.

## APPENDIX

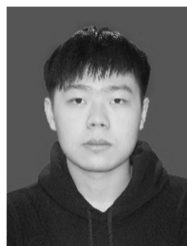
The specific form of  $F_{INS}$  in equation (12) can be expressed as:

$$F_{INS} = \begin{bmatrix} 0 & \mathbf{I} & \mathbf{0} & \mathbf{0} & \mathbf{0} \\ 0 & -2(\boldsymbol{\omega}_{ie}^e) \times & (C_b^e \mathbf{f}_{ib}^b) \times & C_b^e & \mathbf{0} \\ 0 & \mathbf{0} & -(\boldsymbol{\omega}_{ie}^e) \times & \mathbf{0} & -C_b^e \\ 0 & \mathbf{0} & \mathbf{0} & \mathbf{0} & \mathbf{0} \\ 0 & \mathbf{0} & \mathbf{0} & \mathbf{0} & \mathbf{0} \end{bmatrix} \quad (32)$$

## REFERENCES

- [1] P. Yang, D. Duan, C. Chen, X. Cheng and L. Yang, "Multi-Sensor Multi-Vehicle (MSMV) Localization and Mobility Tracking for Autonomous Driving," *IEEE Trans. Veh. Technol.*, vol. 69, no. 12, pp. 14355-14364, Dec. 2020.
- [2] E. Yurtsever, J. Lambert, A. Carballo and K. Takeda, "A Survey of Autonomous Driving: Common Practices and Emerging Technologies," *IEEE Access*, vol. 8, pp. 58443-58469, Aug. 2020.
- [3] S. Kuutti, S. Fallah, K. Katsaros, M. Dianati, F. McCullough, and A. Mouzakitis, "A survey of the state-of-the-art localization techniques and their potentials for autonomous vehicle applications," *IEEE Internet of Things J.*, vol. 5, no. 2, pp. 829-846, Apr. 2018.
- [4] W. Wen, X. Bai, Y. C. Kan and L. Hsu, "Tightly Coupled GNSS/INS Integration via Factor Graph and Aided by Fish-Eye Camera," *IEEE Trans. Veh. Technol.*, vol. 68, no. 11, pp. 10651-10662, Nov. 2019.
- [5] X. Li, M. Ge, X. Dai, X. Ren, M. Fritsche, and J. Wickert, "Accuracy and reliability of multi-GNSS real-time precise positioning: GPS, GLONASS, BeiDou, and Galileo," *J. Geod.*, vol. 89, no. 6, pp. 607-635, Jun. 2015.
- [6] H. He, J. Li, Y. Yang, et al., "Performance assessment of single- and dual-frequency BeiDou/GPS single-epoch kinematic positioning," *GPS Solut.*, vol. 18, no. 3, pp. 393-403, Jul. 2014.
- [7] C. Deng, W. Tang, J. Liu, et al., "Reliable single-epoch ambiguity resolution for short baselines using combined GPS/BeiDou system," *GPS Solut.*, vol. 18, no. 3, pp. 375-386, Jul. 2014.
- [8] Y. Tian, L. Sui, G. Xiao, et al., "Analysis of Galileo/BDS/GPS signals and RTK performance," *GPS Solut.*, vol. 23, no. 2, pp. 1-16, Feb. 2019.
- [9] P. J. G. Teunissen, R. Odolinski, D. Odiijk, "Instantaneous BeiDou + GPS RTK positioning with high cut-off elevation angles," *J. Geod.*, vol. 88, no. 4, pp. 335-350, Apr. 2014.
- [10] F. Zhu, Z. Hu, W. Liu, X. Zhang, "Dual-Antenna GNSS Integrated With MEMS for Reliable and Continuous Attitude Determination in Challenged Environments," *IEEE Sens. J.*, vol. 19, no. 9, pp. 3449-3461, May 2019.
- [11] G. T. Schmidt, R. E. Phillips, "INS/GPS integration architecture performance comparisons," *Low-Cost Navig. Sens. Integr. Technol.*, pp. 1-21, 2011.
- [12] X. Niu, Q. Zhang, L. Gong, et al., "Development and evaluation of GNSS/INS data processing software for position and orientation systems," *Surv. Rev.*, vol. 47, no. 341, pp. 87-98, Apr. 2014.
- [13] H. Han, J. Wang, J. Wang, A. H. Moraleda, "Reliable partial ambiguity resolution for single-frequency GPS/BDS and INS integration," *GPS Solut.*, vol. 21, no. 1, pp. 251-264, Feb. 2016.
- [14] S. Godha, M. E. Cannon, "GPS/MEMS INS integrated system for navigation in urban areas," *GPS Solut.*, vol. 11, no. 3, pp.193-203, Jan. 2007.
- [15] T. Li, H. Zhang, Z. Gao, Q. Chen, X. Niu, "High-accuracy positioning in urban environments using single-frequency multi-GNSS RTK/MEMS-IMU integration," *Remote Sens.*, vol. 10, no. 2, pp. 205, Jan. 2018.
- [16] P. J. Besl, N. D. Mckay, "A method for registration of 3-D shapes," *IEEE Trans. Pattern Anal. Mach. Intell.*, vol. 18, no. 2, Feb. 1992.
- [17] J. Minguez, F. Lamiroux and L. Montesano, "Metric-Based Scan Matching Algorithms for Mobile Robot Displacement Estimation," in *2005 IEEE International Conference on Robotics and Automation (ICRA)*, 2005, pp. 3557-3563.
- [18] A. Segal, D. Haehnel, S. Thrun, "Generalized-ICP," *Robotics: science and systems*, vol. 2, no. 4, 2009.
- [19] J. Zhang, S. Singh, "LOAM: Lidar Odometry and Mapping in Real-time," *Robotics: Science and Systems Conference*, vol.2, no. 9, 2014.
- [20] T. Shan, B. Englott, "LeGO-LOAM: Lightweight and Ground-Optimized Lidar Odometry and Mapping on Variable Terrain," in *2018 IEEE/RSJ International Conference on Intelligent Robots and Systems (IROS)* 2018, pp. 4758-4765.
- [21] Z. Liu, F. Zhang, "BALM: Bundle Adjustment for Lidar Mapping," in *IEEE Robotics and Automation Letters*, vol. 6, no. 2, pp. 3184-3191.
- [22] A. Schütz, D. E. Sánchez-Morales and T. Pany, "Precise positioning through a loosely-coupled sensor fusion of GNSS-RTK, INS and LiDAR for autonomous driving," in *2020 IEEE/ION Position, Location and Navigation Symposium (PLANS)*, 2020, pp. 219-225.
- [23] K. -W. Chiang, G. -J. Tsai, H. -J. Chu and N. El-Sheimy, "Performance Enhancement of INS/GNSS/Refreshed-SLAM Integration for Acceptable Lane-Level Navigation Accuracy," *IEEE Trans. Veh. Technol.*, vol. 69, no. 3, pp. 2463-2476, March 2020.
- [24] T. Shan, B. Englott, D. Meyers, W. Wang, C. Ratti and D. Rus, "LIO-SAM: Tightly-coupled Lidar Inertial Odometry via Smoothing and Mapping," in *2020 IEEE/RSJ International Conference on Intelligent Robots and Systems (IROS)*, 2020, pp. 5135-5142.
- [25] A. Soloviev, "Tight Coupling of GPS and INS for Urban Navigation," *IEEE Trans. Aerosp. Electron. Syst.*, vol. 46, no. 4, pp. 1731-1746, Oct. 2010.
- [26] X. Li, H. Wang, S. Li, et al., "GIL: a tightly coupled GNSS PPP/INS/LiDAR method for precise vehicle navigation", *Satell. Navig.*, vol. 2, no. 1, pp. 1-17, Nov. 2021.

- [27] W. Li, G. Liu, X. Cui, M. Lu, "Feature-Aided RTK/LiDAR/INS Integrated Positioning System with Parallel Filters in the Ambiguity-Position-Joint Domain for Urban Environments", *Remote Sens.*, vol. 13, no. 10, May 2021.
- [28] X. Zhang, F. Zhu, Y. Zhang, et al., "The improvement in integer ambiguity resolution with INS aiding for kinematic precise point positioning", *J. Geod.*, vol. 93, no. 7, pp. 993-1010, Dec. 2018.
- [29] A. Brack, "Reliable GPS+ BDS RTK positioning with partial ambiguity resolution", *GPS solut.*, vol. 21, no. 3, pp. 1083-1092, Dec. 2016.
- [30] P. J. G Teunissen, "The least-squares ambiguity decorrelation adjustment: A method for fast GPS integer ambiguity estimation", *J. Geod.*, vol. 70, no. 1-2, pp. 65-82, Nov. 1995.
- [31] F. Azevedo et al., "Real-Time LiDAR-based Power Lines Detection for Unmanned Aerial Vehicles," in *2019 IEEE International Conference on Autonomous Robot Systems and Competitions (ICARSC)*, 2019, pp. 1-8.
- [32] E. Ermerfeldt, "Fitting a plane to noisy points in 3d," [Online]. Available: [http://www.ilikebigbits.com/2017\\_09\\_25\\_plane\\_from\\_points\\_2.html](http://www.ilikebigbits.com/2017_09_25_plane_from_points_2.html)
- [33] W. Lee, Y. Yang, and G. Huang, "Efficient Multi-sensor Aided Inertial Navigation with Online Calibration," in *2021 IEEE International Conference on Robotics and Automation (ICRA)*, 2021, pp. 5706-5712.
- [34] J. S. Beis, D. G. Lowe, "Shape indexing using approximate nearest-neighbour search in high-dimensional spaces," in *Proceedings of IEEE Computer Society Conference on Computer Vision and Pattern Recognition*, 1997, pp. 1000-1006.
- [35] P. Groves, "INS/GNSS Integration," in *Principles of GNSS, Inertial, and Multisensor Integrated Navigation Systems*, 2nd ed., London, UK: Artech House, 2013, pp. 363-406.
- [36] A. I. Mourikis, S. I. Roumeliotis, "A Multi-State Constraint Kalman Filter for Vision-aided Inertial Navigation," in *Proceedings 2007 IEEE International Conference on Robotics and Automation (ICRA)*, 2007, pp. 3565-3572.
- [37] J. Lv, J. Xu, K. Hu, Y. Liu, X. Zuo, "Targetless Calibration of LiDAR-IMU System Based on Continuous-time Batch Estimation," in *2020 IEEE/RSJ International Conference on Intelligent Robots and Systems (IROS)*, 2020, pp. 9968-9975.
- [38] X. Li, X. Li, J. Huang, Z. Shen, B. Wang, Y. Yuan and K. Zhang, "Improving PPP-RTK in urban environment by tightly coupled integration of GNSS and INS," *J. Geod.*, vol. 95, no. 132, Nov. 2021.
- [39] K. Sun et al., "Robust Stereo Visual Inertial Odometry for Fast Autonomous Flight," in *IEEE Robotics and Automation Letters*, vol. 3, no. 2, pp. 965-972, Apr. 2018.
- [40] P. J. G Teunissen, P. J. de Jonge, C. C. J. M. Tiberius, "The Volume of the GPS Ambiguity Search Space and its Relevance for Integer Ambiguity Resolution," in *Proc. ION GPS*, 1996, vol. 9, pp. 889-898.



**Shengyu Li** received the B.S. degree in geodesy and survey engineering from Wuhan University, Wuhan, China, in 2019.

He is currently a doctor candidate at the school of Geodesy and Geomatics, Wuhan University. His current research focuses on integrated navigation system, multi-sensor fusion.



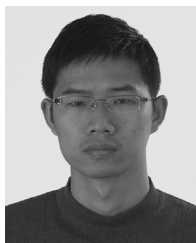
**Yuxuan Zhou** received the B.S. degree in geodesy and survey engineering from Wuhan University, Wuhan, China, in 2019.

He is currently a doctor candidate at the school of Geodesy and Geomatics, Wuhan University. His current research focuses on integrated navigation system, multi-sensor fusion.



**Chunxi Xia** received the B.S. degree in geodesy and survey engineering from Wuhan University, Wuhan, China, in 2020.

He is currently a master candidate at the school of Geodesy and Geomatics, Wuhan University. His current research focuses on vision-based navigation, multi-sensor fusion.



**Xingxing Li** is currently a professor at the Wuhan University. He has completed his B.Sc. degree at the school of Geodesy and Geomatics in Wuhan University. He obtained his Ph.D. degree at the Department of Geodesy and Remote Sensing of the German Research Centre for Geosciences (GFZ). His current research mainly involves GNSS precise data processing and multi-sensor fusion.



**Shiwen Wang** received the B.S. degree navigation engineering from Wuhan University, Wuhan China, in 2021.

He is currently a master candidate at the school of Geodesy and Geomatics, Wuhan University. His current research focuses on integrated navigation system, GNSS precise positioning.



**Zhiheng Shen** received the B.S. degree in geodesy and survey engineering from Wuhan University, Wuhan, China, in 2019.

He is currently a doctor candidate at the school of Geodesy and Geomatics, Wuhan University. His current research focuses on integrated navigation system, GNSS precise positioning.